



Study on the failure mechanism of clay layer overlying thin bedrock in coal seam mining

Guangming Wu¹ · Haibo Bai¹ · Bin Du^{1,2} · Luyuan Wu¹ · Shixin He¹ · Hao Li¹

Received: 8 May 2018 / Accepted: 29 April 2019 / Published online: 14 May 2019
© Springer-Verlag GmbH Germany, part of Springer Nature 2019

Abstract

The water-blocking property of clay at the bottom of the Cenozoic overburden is an important factor for mining safety and protecting underground latent water resources in thin bedrock coal seam mining. The failure mechanism of such a clay is studied based on the actual engineering background of the SanYuan Coal Mine. The failure of the overlying clay layer is due to the reduction in the supporting space of the clay layer with the progression of coal mining, and the overlying clay layer will subside due to the self-weight load. Therefore, the vertical stress, horizontal stress and shear stress of the soil change during subsidence, and the change in these stresses determine whether the clay layer fails. Then, the failure criterion of soil expressed by the vertical stress, horizontal stress and shear stress is derived based on Mohr–Coulomb shear failure theory. Next, the function relating the stress and subsidence magnitudes are established by fit analysis. Finally, a failure criterion expressed in terms of soil subsidence amount is presented. Based on the failure criterion expressed by soil subsidence amount, a method for soil failure discriminant is proposed, in which only the subsidence amount is necessary to judge the soil failure state. This method is applied to the engineering of the SanYuan Coal Mine to get the failure subsidence amount curve of clay layer I. The results show that the failure subsidence amount curve plots below the subsidence amount curves of clay layer I at any advancing distance; that is, the clay layer did not fail. An investigation of the source and amount of water inflow to the 3301 working face also verifies that the clay layer does not fail, and the failure discriminant method used to judge the failure state of the soil is appropriate and convenient for use in engineering applications.

Keywords Thick overburden · Coal mining · Clay failure mechanism · Thin bedrock

Introduction

Environmental problems, such as a shortage of water resources and surface degradation caused by coal mining, are becoming increasingly prominent as the intensity of coal mining in China increases. This is especially true in the mid-west areas, where underground latent water resources are widely distributed in the Cenozoic overburden. The damage of underground latent water resources is particularly evident in the coal seam mining process (Zhang et al. 2010a, 2017; Bai et al. 2013). Therefore, ideas and methods, such

as “Green Coal Mining (Qian et al. 2003, 2006; Qian 2010)” and the “Coexistence of Coal and Water (Fan 2005, 2011; Fan et al. 2009)”, have been proposed. These ideas and methods have provided new methods for the protection of underground latent water resources (Ma et al. 2016a, 2017).

To find solutions to specific problems, such as maintaining the safety of coal seam mining and researching the water-blocking mechanisms of rock or clay, scholars in China and abroad have carried out a series of useful studies by establishing safety assessment methods, conducting field measurements and running numerical simulations (Ma et al. 2016b). For example, put forward the concept of the risk coefficient of water inrush in loose porous aquifers and the clay at the bottom of the Quaternary system can be used as part of the mining protection layer (Meng et al. 2013; Sun et al. 2004; Dong and Cai 2006; Zhou et al. 2018a, 2019; Du et al. 2013). These studies provide guidance to improve the extent of coal seam mining under thin bedrock. Simultaneously, the problem of mining subsidence in thick

✉ Haibo Bai
hbbaiteacher@sina.com

¹ State Key Laboratory for Geomechanics and Deep Underground Engineering, China University of Mining and Technology, Xuzhou 221116, Jiangsu, China

² Jiangsu Vocational Institute of Architectural Technology, Xuzhou 221116, Jiangsu, China

loose overburden deserves attention, and some scholars have proposed new methods of subsidence prediction for thick unconsolidated layers based on field test data (Yang and Xia 2013; Zhou et al. 2016).

Much research has also been conducted on the protection of water resources. The influence of coal mining on underground latent water resources was divided into four categories: serious, moderate, slight, and no water loss, and an aquifer-protection mining technique can be successfully applied by modifying a few mining parameters, such as mining height or advance rate. Meanwhile, the key factor in protecting underground latent water resources is the thickness of the weathered bedrock located immediately below the aquifer (Zhang et al. 2011; Qiao et al. 2017; Xu et al. 2018). Mining activities can cause not only surface and subsurface water loss but also chemical, trace metal and microbiological pollution of surface and subsurface water (Tiwary 2001; Dhakate et al. 2008; Ma et al. 2019; Arkoc et al. 2016).

The failure of bedrock in thin bedrock coal seam mining has obvious dynamic pressure and bench convergence characteristics, which are different from the failure of coal seam mining under normal thickness bedrock, and the development of water flowing fractured zone is also different from that of normal thickness bedrock (Du et al. 2013; Palchik 2003; Xuan 2008; Yang and Xia 2018).

The clay layer at the bottom of the Cenozoic overburden is an important water-blocking structure in the case with water flowing fractured zone penetrate through the thin bedrock and plays an important role in preventing water in porous aquifers and phreatic aquifers from flowing to the working face (Ma et al. 2016b, 2018). In addition, the properties, distribution characteristics and mining failure characteristics of clay have important influences on the water-blocking performance of clay (Zhang et al. 2010b; Li et al. 2017; Xu 2004a). Determining the failure law of clay layer over thin bedrock and the clay water-blocking mechanism are new problems that need to be solved (Zhou et al. 2018b). At present, the answers to these problems are still being explored by laboratory testing and numerical simulation. For example, one study found that the failure of clay aquifuge is a gradual process and it has a threshold effect, which is presented based on physical simulations (Zhang et al. 2018).

This paper analyses the failure mechanism of clay in coal seam mining under thin bedrock by combining theoretical analyses and numerical simulations based on the geological conditions of mining area No. 3 in the SanYuan Coal Mine. Additionally, the water inflow was observed during mining of the 3301 working face, and a water quality test was performed, both of which were used as verifying methods.

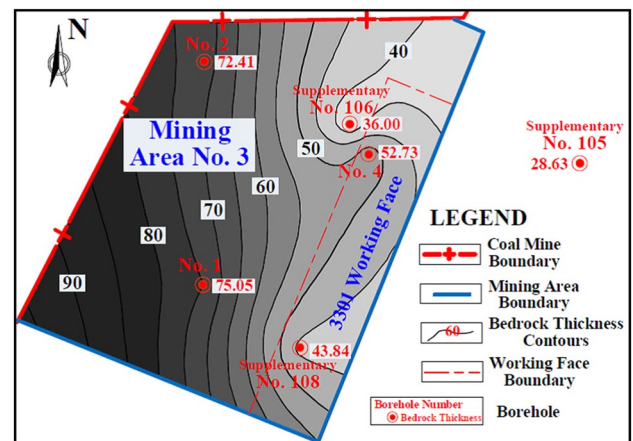


Fig. 1 The contour map of the bedrock thickness

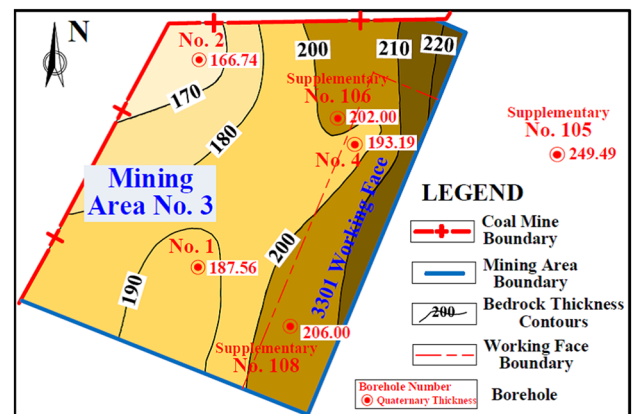


Fig. 2 The contour map of the Quaternary overburden thickness

General situation of engineering geology

The SanYuan Coal mine is located in the ChangZhi Basin, which is in the southeastern part of the QinShui Coal Field. The Quaternary overburden fully covers this area, and the dip angle of the stratum is generally less than 8° . The basic geological conditions of mining area No. 3 are as follows. First, the thickness of the No. 3 coal seam is 6.7–7.5 m, and the bedrock thickness is 36.0–75.1 m (Fig. 1). The thickness of the Quaternary overburden is 166.7–206.6 m (Fig. 2). Second, the bedrock is thinner in the east and thicker in the west, while the distribution of the Quaternary overburden is opposite to that of the bedrock.

The 3301 working face, which was the first to be exploited, is located in the eastern region of mining area No. 3. The bedrock thickness is less than 50 m, while the thickness of the Quaternary overburden is greater than 200 m in most areas of the 3301 working face. According to the classifications of bedrock thickness given in the relevant literature (Fang et al. 2008), (1) if the bedrock thickness is

less than the height of the caving zone, it is called ultrathin bedrock; (2) if the bedrock thickness is greater than the height of the caving zone and less than the height of the water flowing fractured zone, it is called thin bedrock; and (3) if the bedrock thickness is greater than the height of the water flowing fractured zone, it is called normal thickness bedrock. Therefore, the coal seam in the 3301 working face is exploited under the typical geological conditions of a thin bedrock and a thick overburden.

The Quaternary overburden in the mining area No. 3 is mainly composed of clay or silty clay and has a reddish brown or yellowish brown colour. The Quaternary overburden has multiple porous aquifers that are moderately water-rich and are mainly composed of sand. The clay layers and porous aquifers are stratiform interphase, as shown in Fig. 3. The porous aquifer near the surface is a phreatic aquifer and extremely water-rich, with a great capacity for water storage. Therefore, surface water ponds, which are shown in Fig. 4, have formed in low-lying areas or by manual excavation due to the subsurface water level emerge naturally. The catchment area of the largest water pond is approximately 105,740 m², and the volume of water is approximately 191,682 m³.

Theoretical analysis of clay failure

Basic clay properties

According to the tests conducted on the samples, the soil of the Quaternary overburden has the following basic characteristics. (1) This soil is mainly composed of clay with a plasticity index greater than 17 and, to a lesser degree, silty clay with a plasticity index between 10 and 17. (2) The coefficient of the vertical permeability of the clay is less than 10⁻⁴ cm/s and decreases to 10⁻⁶–10⁻⁸ cm/s as the burial depth increases, as shown in Table 1. That is, this clay is low-permeability or extremely low-permeability clay. (3) The liquidity index of most shallow clays are between 0 and 0.75, which are in a plastic or hard plastic state. At the same time, the liquidity index of most deeper clays are less than or equal to 0, which are in a hard state (shown in Fig. 5).

According to related research (Li et al. 2017; Xu 2004b; Liu 2016; Chen 1997), clay with the above-mentioned properties is generally favourable to use in engineering geology because it has well water-blocking performance before failure.

The stress–strain relationship obtained by unconfined compressive strength tests are shown in Fig. 6; clearly, the unconfined compressive strength and the corresponding axial strain of the soil specimens vary with burial depth. The clay has a post-peak effect and still has considerable residual strength after reaching peak strength when the

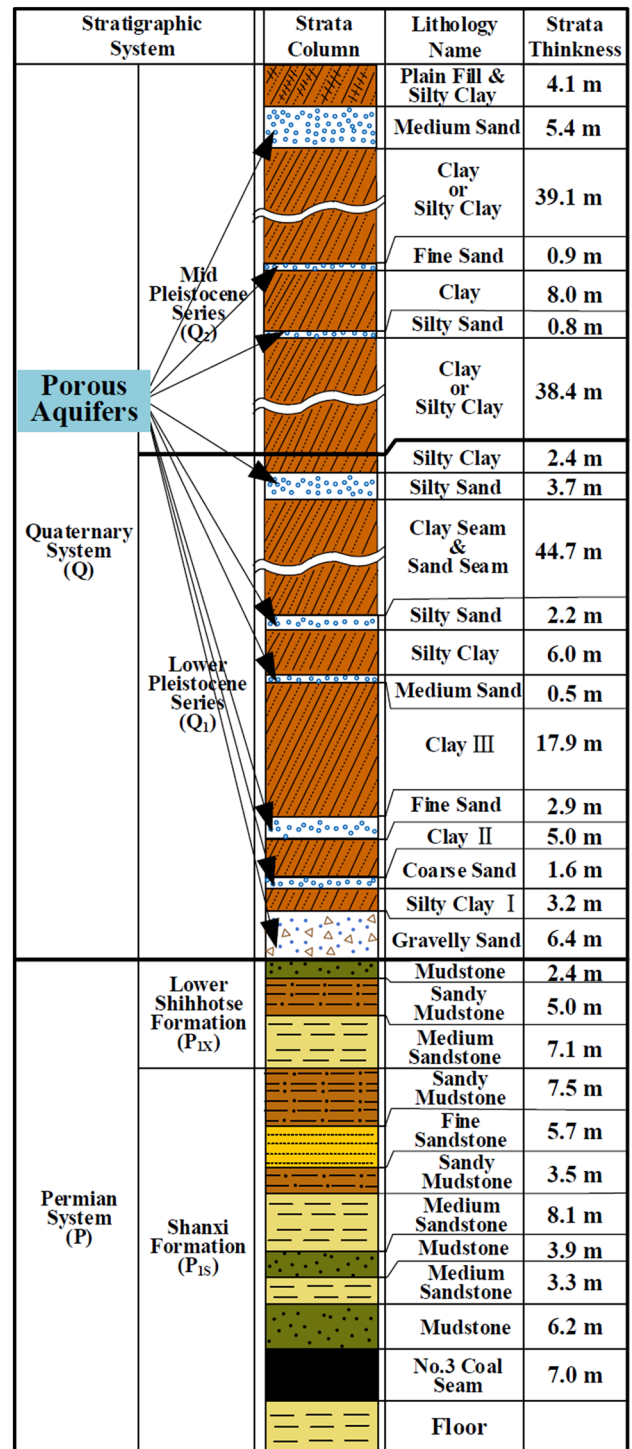


Fig. 3 Stratigraphic column of No. 4 borehole

burial depth is less than 101.5 m. In contrast, when the burial depth is greater than 142.8 m, the strain that clay can bear decreases and the clay will rapidly undergo failure after reaching its peak strength. Therefore, shallow clay has obvious plastic characteristics and can withstand relatively



Fig. 4 Surface water ponds formed in low-lying areas or by manual excavation

strong deformation, while deeper clay exhibits brittle characteristics and is unable to withstand large deformation. In addition, the unconfined compressive strength of the clay significantly improves with increasing burial depth; the unconfined compressive strength of the clay buried to

162.9 m is 334.43 kPa, which is 5 times that of the clay buried to 42.7 m.

Failure mechanism of clay

The clay layer that overlies the thin bedrock will deform or even fail with the deformation and caving of the bedrock as the coal seam is continuously exploited, as shown in Fig. 7. The process of deformation or failure of the overlying soil layer can be divided into three stages. First, the coal seam is mined out. Second, the bedrock collapses or fractures. Third, the collapse or fracture of the thin bedrock leads to the reduction in the supporting space of the overlying soil layers, and the overlying soil layers will subside due to the self-weight load. Then, the overlying soil layers undergo deformation or failure. Consequently, the essential cause of the deformation or failure of the clay layer is the reduction in the supporting space in its lower part.

The overlying soil layer will subside due to the self-weight load when the supporting space decreases; consequently, the normal stress and shear stress in an arbitrary section at each point in the soil changes before the overlying soil layer is re-compacted on the collapsed or cracked bedrock. Shear deformation occurs in the soil due to the shear stress, and shear failure occurs if the shear stress in a certain section plane of the soil reaches the shear strength (Su 2015).

Coulomb put forward a formula for the shear strength of soil based on direct shear test results.

$$\tau = \sigma \tan \phi + c, \quad (1)$$

where τ is the shear stress acting on the shear failure plane, σ is the normal stress acting on the shear failure plane, ϕ is the internal friction angle of the soil, and c is the cohesion of the soil in Formula (1).

On the basis of Coulomb's research, Mohr put forward the theory that materials fail by shear failure and that there is a certain functional relationship between shear stress and normal stress on the failure plane, which is described by Formula (2).

Table 1 Properties of the clay samples

Samples number	Burial depth (m)	Density (g/cm^3)	Cohesion (kPa)	Internal friction angle ($^\circ$)	Vertical permeability coefficient (cm s^{-1})
2–20	27.8	1.94	70.7	21.2	1.60×10^{-4}
2–27	42.7	1.90	46.8	21.9	–
2–50	66.7	1.93	105.3	21.3	2.12×10^{-7}
2–69	87.9	2.05	–	–	4.85×10^{-7}
2–80	121.8	2.03	162.0	28.6	–
2–83	142.8	1.98	–	–	5.33×10^{-8}
2–84	154.4	2.15	104.5	29.1	4.95×10^{-8}

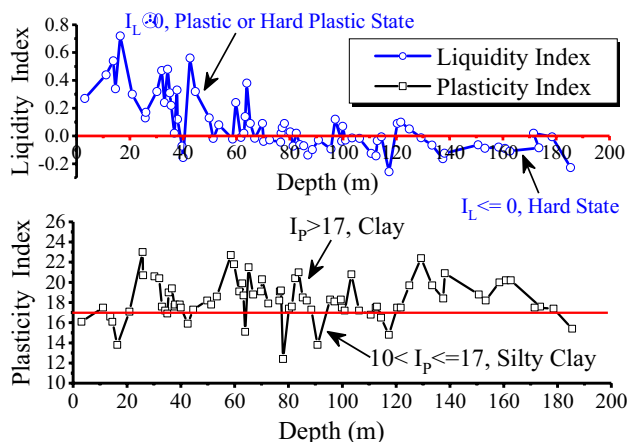


Fig. 5 Relationship between clay liquidity/plasticity index and burial depth

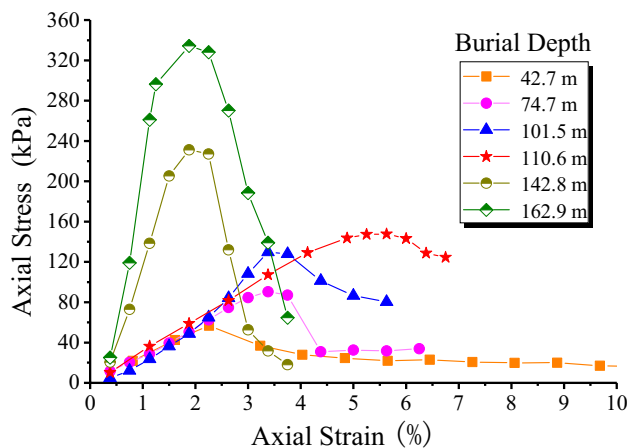


Fig. 6 Unconfined compressive strength curve of the soil specimens

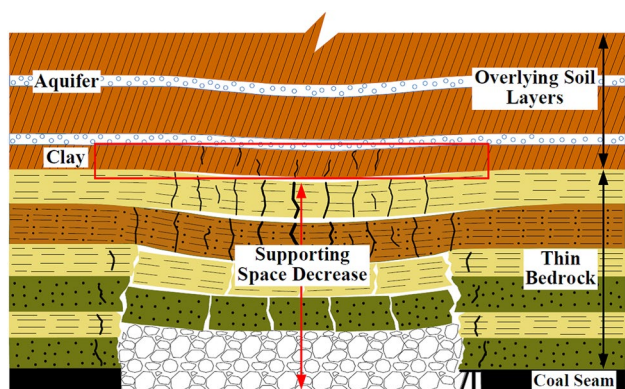


Fig. 7 Sketch map of the deformation and failure of clay

$$\tau = f(\sigma). \tag{2}$$

The failure criterion of the above-mentioned Mohr–Coulomb strength theory is based on whether the shear stress

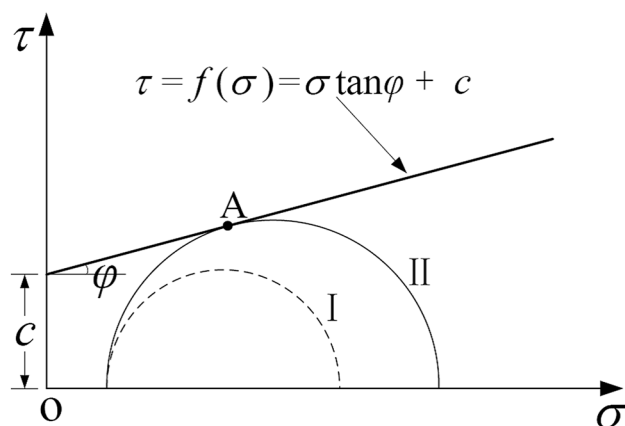


Fig. 8 Discrimination of the soil failure state

reaches the shear strength of soil. According to Mohr–Coulomb strength theory, the Mohr–Coulomb shear strength envelope can be drawn in the same coordinate space as the Mohr stress circle. Then, it can be determined whether the soil fails on the basis of the relationship between the Mohr–Coulomb shear strength envelope and the Mohr stress circle, as shown in Fig. 8.

When the Mohr stress circle (round I in Fig. 8) plots below the shear strength envelope, that is, the shear stress at any section plane in the soil is less than the shear strength of the soil, the soil will not experience shear failure. If the Mohr stress circle is tangent to the shear strength envelope (round II in Fig. 8) at tangent point A, the shear stress acting on the section plane of point A is equal to the shear strength of the soil, and the soil is in the ultimate equilibrium state. The Mohr stress circle under this condition is called the ultimate stress circle.

Failure criterion expressed by soil subsidence amount

The ultimate equilibrium conditions of shear failure expressed by the maximum principal stress σ_1 and minimum principal stress σ_3 can be established according to the geometric relationship between the ultimate stress circle and the shear strength envelope, as shown in Fig. 9.

The shear strength envelope intersects the σ axis at point O'' , and the shear failure ultimate equilibrium conditions expressed by the maximum principal stress σ_1 and minimum principal stress σ_3 can be obtained from geometric relations of the right triangle $O'AO''$.

$$\sin \varphi = \frac{\overline{O'A}}{\overline{O'O''}} = \frac{\frac{\sigma_1 - \sigma_3}{2}}{\frac{c}{\tan \varphi} + \frac{\sigma_1 + \sigma_3}{2}}. \tag{3}$$

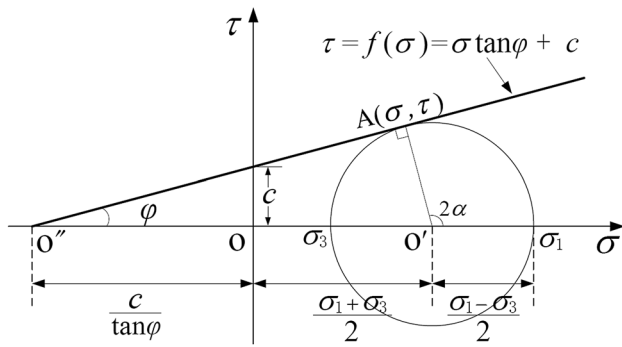


Fig. 9 Limit equilibrium conditions of soil failure

Simplifying Formula (3) gives

$$\sigma_1 - \sigma_3 \frac{1 + \sin \varphi}{1 - \sin \varphi} - \frac{2c \cos \varphi}{1 - \sin \varphi} = 0. \tag{4}$$

The trigonometric function transform of Formula (4) gives

$$\sigma_1 - \sigma_3 \tan^2 \left(\frac{\pi}{4} + \frac{\varphi}{2} \right) - 2c \tan \left(\frac{\pi}{4} + \frac{\varphi}{2} \right) = 0. \tag{5}$$

Formula (5) represents the relationship between the maximum principal stress σ_1 , minimum principal stress σ_3 , internal friction angle ϕ and cohesion c of a soil unit in its ultimate equilibrium state. Therefore, the relationship between σ_1 , σ_3 , ϕ and c should satisfy the conditions shown in Formula (6) to ensure that the soil is not failing.

$$\sigma_1 - \sigma_3 \tan^2 \left(\frac{\pi}{4} + \frac{\varphi}{2} \right) - 2c \tan \left(\frac{\pi}{4} + \frac{\varphi}{2} \right) < 0. \tag{6}$$

The geometric relationship between the stress components in each section plane of a point in the soil can be expressed by the Mohr stress circle (Su 2015), and the stress state of the soil unit is shown in Fig. 10. Points A and B are drawn according to coordinates (σ_z, τ_{zx}) and (σ_x, τ_{xz}) . The Mohr stress circle is drawn with the midpoint C along the line segment AB and the diameter of line segment AB (Fig. 10). $\tau_{zx} = -\tau_{xz}$ by the shear stress reciprocity theorem.

The Mohr stress circle intersects the σ axis at points D and E, and the shear stress at these two points is zero. Simultaneously, the positive stress at point D is the maximum principal stress σ_1 of the unit, and the positive stress at point E is the minimum principal stress σ_3 of the unit. Then, σ_1 and σ_3 can be calculated by Formulas (7) and (8) on the basis of the geometric relationship.

$$\sigma_1 = \frac{\sigma_z + \sigma_x}{2} + \sqrt{\left(\frac{\sigma_z - \sigma_x}{2} \right)^2 + \tau_{zx}^2} \tag{7}$$

$$\sigma_3 = \frac{\sigma_z + \sigma_x}{2} - \sqrt{\left(\frac{\sigma_z - \sigma_x}{2} \right)^2 + \tau_{zx}^2}. \tag{8}$$

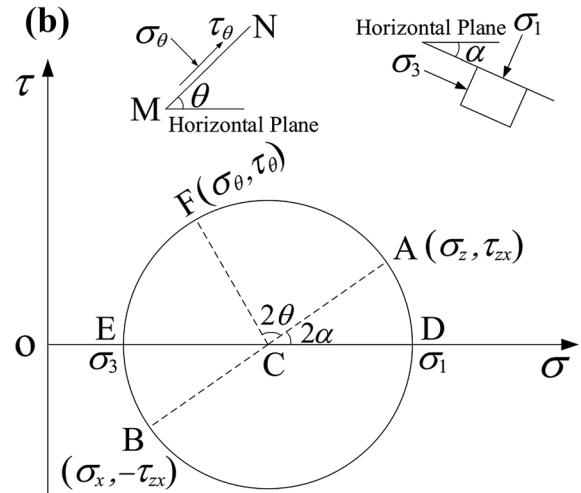
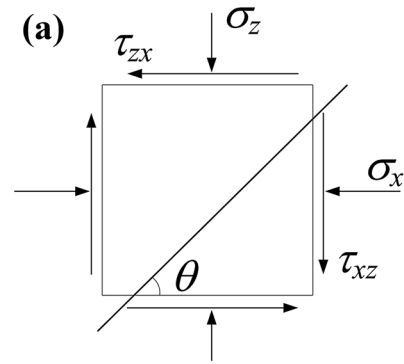


Fig. 10 Mohr stress circle of a soil unit: a stress state of the soil unit; b Mohr stress circle

Substituting Formulas (7) and (8) into Formula (6), the relationship between σ_z , σ_x , τ_{zx} , ϕ and c is obtained when the soil is not failing, as given in Formula (9).

$$\frac{\sigma_z + \sigma_x}{2} \left[1 - \tan^2 \left(\frac{\pi}{4} + \frac{\varphi}{2} \right) \right] + \sqrt{\left(\frac{\sigma_z - \sigma_x}{2} \right)^2 + \tau_{zx}^2} \left[1 + \tan^2 \left(\frac{\pi}{4} + \frac{\varphi}{2} \right) \right] - 2c \tan \left(\frac{\pi}{4} + \frac{\varphi}{2} \right) < 0. \tag{9}$$

Let $\tan \left(\frac{\pi}{4} + \frac{\varphi}{2} \right)$ be factor ζ ; then, Formula (9) can be simplified to Formula (10).

$$(1 - \zeta^2) \frac{\sigma_z + \sigma_x}{2} + (1 + \zeta^2) \sqrt{\left(\frac{\sigma_z - \sigma_x}{2} \right)^2 + \tau_{zx}^2} - 2c\zeta < 0. \tag{10}$$

Formula (10) shows that the change of vertical stress σ_z , horizontal stress σ_x and shear stress τ_{zx} determine whether the soil is in failure. The soil subsidence, which is caused by coal seam mining, leads to the change of vertical stress σ_z , horizontal stress σ_x and shear stress τ_{zx} . Thus, the functional relationship between soil subsidence amount Δz and

Table 2 Physical and mechanical parameters of the model

Lithology	Modulus of elasticity (GPa)	Poisson’s ratio	Cohesion (MPa)	Tensile strength (MPa)	Internal friction angle (°)	Density (kg/m ³)
Sand	10 kPa	–	200 Pa	200 Pa	20.0	1690
Clay	0.021	0.35	0.162	0.195	28.6	1990
Fine sandstone	38.0	0.25	5.91	1.98	24.4	2744
Medium sandstone	35.0	0.25	5.20	1.09	30.5	2672
Sandy mudstone	16.3	0.26	3.45	0.59	29.0	2548
Mudstone	12.1	0.28	2.30	0.47	20.9	2640
Coal	5.0	0.23	2.03	0.31	43.0	1600
Floor	35.00	0.25	5.20	1.52	30.5	2672

vertical stress σ_z , horizontal stress σ_x and shear stress τ_{zx} can be established:

$$\sigma_z = f_z(\Delta z), \sigma_x = f_x(\Delta z), \tau_{zx} = f_\tau(\Delta z). \tag{11}$$

Formula (12) can be obtained by substituting Formula (11) into Formula (10).

$$(1 - \zeta^2) \frac{f_z(\Delta z) + f_x(\Delta z)}{2} + (1 + \zeta^2) \sqrt{\left(\frac{f_z(\Delta z) - f_x(\Delta z)}{2}\right)^2 + f_\tau^2(\Delta z)} - 2c\zeta < 0. \tag{12}$$

Formula (12) is the failure criterion of soil expressed by subsidence amount Δz and is a single-variable expression. This criterion can provide a new method for judge the failure conditions of the clay in thin bedrock coal seam mining.

Numerical analysis of the failure of clay

This section aims to establish the functional relationship between soil subsidence amount and the corresponding stress in thin bedrock coal seam mining by numerical analysis, and the software used is FLAC^{3D} (ITASCA Consulting Group, USA). Then, the failure criterion that is expressed in terms of subsidence amount is established according to the fit functional relationship between subsidence amount and stress.

Build model

A model with brick units is generated, and the total number of units in the model is 501,760. The constitutive model of the geomaterials is the Mohr–Coulomb plastic model, which is a general constitutive model suitable for typical rocks and soils and is widely used in underground excavation design, slope stability analysis and other fields. FLAC^{3D} is a finite difference software that adopts the numerical calculation method of the fast Lagrangian analysis of a continuum.

Therefore, it does not allow unit separation and shedding, and the difference in the coordinate values of the unit mesh nodes is no greater than 1×10^{-7} .

The size of the model in the x , y , and z directions, which were modelled on the basis of the stratigraphic column shown in Fig. 3, is 490 m \times 320 m \times 282 m (length \times width \times height), and the physical and mechanical parameters of each rock and soil layer are shown in Table 2. The mechanical parameters in Table 2 are derived partly from laboratory tests and partly from the existing literature. The mechanical parameters obtained from the laboratory tests are as follows: the cohesion, internal friction angle and density of the clay and the tensile strength and density of the rocks. Other mechanical parameters that cannot be obtained directly due to the limitation of the test conditions are obtained from relevant references (Du et al. 2013; Fang et al. 2008; Jiao et al. 2012), and the mechanical parameters recorded in the relevant literature were obtained from adjacent coal mines under the same geological conditions in the same mining area. Each rock and soil layer are built as a horizontal stratum because the dip angles of the strata are less than 8° (see Fig. 11).

The x direction of the model is the advancing direction of the working face; the model has a length of 490 m, and the boundary is 50 m on both sides in x direction of the model. The y direction is the working face length direction, and its length is 320 m; however, because the actual length of the 3301 working face is 220 m, and the boundary is 50 m on both sides in y direction of the model. The z direction is vertical, and the model height is 282 m, which contains the 30 m floor, 7 m coal seam, 52 m bedrock and 193 m overburden.

Reserved boundaries are set between the front, back, left, right, bottom and research area (that is, the overlying soil layers) of the model; therefore, the front ($Y=0$ m), back ($Y=320$ m), left ($X=0$ m), right ($X=490$ m) and bottom ($Z=0$ m) of the model are set as displacement boundaries that restrict the normal displacement, which is to prevent the overall movement of the model. The boundary conditions

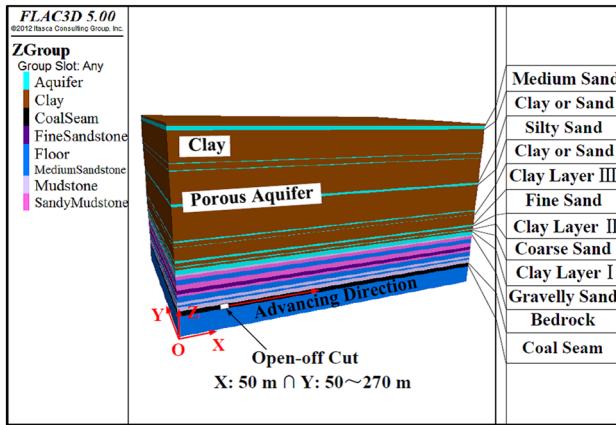


Fig. 11 Numerical simulation model

are set as follows: (1) the bottom ($Z=0$ m) of the model has a displacement boundary condition that restricts the normal displacement and the top ($Z=282$ m) of the model is the surface, which is a free boundary, consistent with the real condition. (2) The front ($Y=0$ m) and back ($Y=320$ m) of the model have displacement boundary conditions that restrict the normal displacement. Similarly, the left ($X=0$ m) and right ($X=490$ m) of the model are have displacement boundary conditions that restrict the normal displacement.

In the simulated excavation, the open-off cut is at the left 50 m of the model. One step is 15 m, and excavation gradually continues to the right along the x direction, 26 excavation steps are applied in total. The measurement points are located along the x direction in each rock or clay stratum, and each measurement point is at the midpoint of the y direction. A diagram of the measurement point arrangement is shown in Fig. 12.

Analysis of the relationship between the clay subsidence amount and stress

The change of the clay stress is mainly caused by mining-affected deformation; thus, a function relationship between subsidence amount Δz and its corresponding vertical stress σ_z , horizontal stress σ_x or shear stress τ_{zx} of the clay can be determined; then, the failure criterion formula expressed by subsidence amount Δz can be presented. The formula provides a new method for analysing whether clay is in a state of failure.

The subsidence amount curves of clay layer I, which is at the bottom of the Quaternary system, are shown in Fig. 13 for different advancing distances.

Figure 13 shows that the subsidence amount of clay layer I has the following characteristics. First, the subsidence amount curve is relatively gentle when the advancing distance is less than 120 m, and the subsidence amount curve

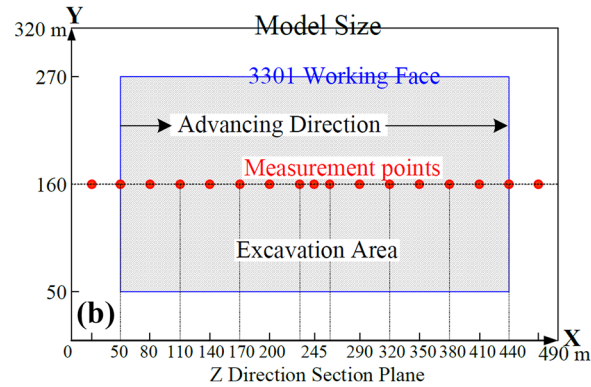
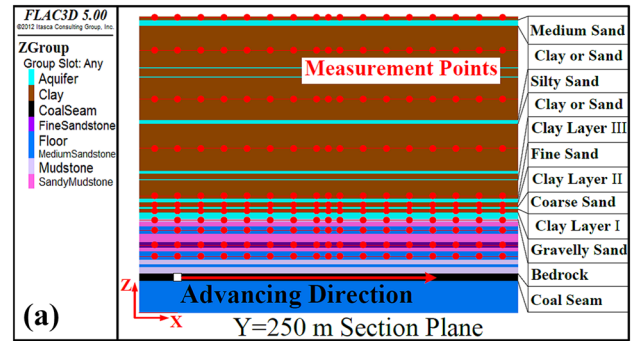


Fig. 12 Arrangement diagram of the measurement points: **a** $Y=250$ m section plane; **b** section plane perpendicular to the z direction

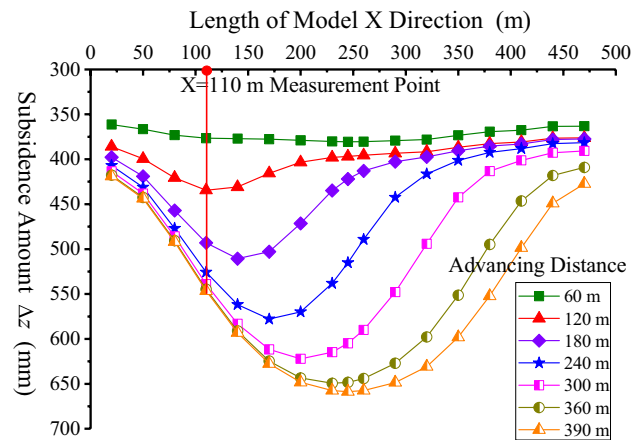


Fig. 13 Subsidence amount curve of clay layer I

varies sharply when the advancing distance is greater than 180 m. Second, the maximum subsidence point moves forward as the advancing distance of the working face increases, and the final subsidence amount curve is U-shaped.

1. Relationship between the shear stress τ_{zx} and subsidence amount Δz

The shear stress τ_{zx} values of each measurement point in clay layer I are shown in Fig. 14 for different advancing distances.

As shown in Fig. 14, the variation laws of the shear stress distribution curves are basically the same at different advancing distances. Meanwhile, the shear stress at the left side of the model, when the x coordinate is less than 170 m, is negative, and the shear stress at each measurement point in the middle and right side of the model (x coordinate greater than 170 m) has a positive value or negative value. Another observation is that mining has a great influence on change in the shear stress, and the variation in shear stress affected by mining is in the range -82.16 to 634.16% .

Taking the advancing distance as the abscissa and the subsidence amount Δz and shear stress τ_{zx} as the ordinates, the corresponding relation between subsidence amount Δz and shear stress τ_{zx} is shown in Fig. 15. This figure shows the corresponding relationship between the subsidence amount and the shear stress at the $X=110$ m measurement point in clay layer I.

Hence, a scatter diagram is plotted, in which the subsidence amount values Δz at the $X=110$ m measurement point are independent variables and its corresponding shear stress τ_{zx} values are dependent variables. We can then fit and analyse their functional relation and establish their fit function expressions. For instance, the scatter diagram and best-fit curve between subsidence amount Δz and its corresponding shear stress τ_{zx} at the $X=110$ m measurement point are shown in Fig. 16. A quartic polynomial [as shown in Formula (13)] and GaussAmp nonlinear function [as shown in Formula (14)] are used for the fit analysis.

$$y = A + B_1 \cdot x + B_2 \cdot x^2 + B_3 \cdot x^3 + B_4 \cdot x^4 \tag{13}$$

$$y = y_0 + Ae^{-\frac{(x-x_0)^2}{2w^2}} \tag{14}$$

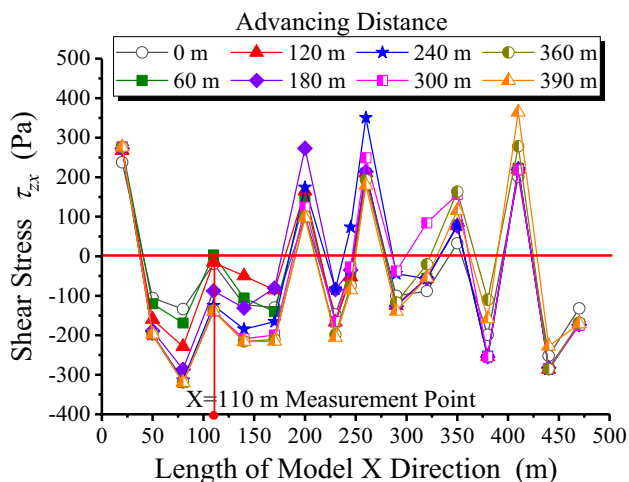


Fig. 14 Shear stress values of each measurement point in clay layer I

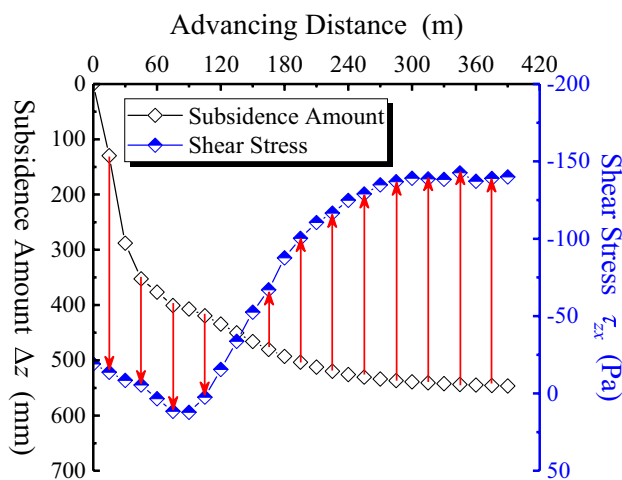


Fig. 15 The relationship between subsidence amount and shear stress

The adjusted determination coefficient R_{adj}^2 and residual scatter diagram of the Quartic polynomial fit and GaussAmp nonlinear fit analysis are shown in Fig. 17, which shows that the R_{adj}^2 determined by the quartic polynomial fit is greater than that of the GaussAmp nonlinear fit, while the residual values of the quartic polynomial fit are lesser than those of the GaussAmp nonlinear fit. This result illustrates that the quartic polynomial fit has a better fit effect than the GaussAmp nonlinear fit in the shear stress fit analysis.

The fit function expressions between the subsidence amount Δz and shear stress τ_{zx} at $X=110$ m measurement point is shown in Formula (15) according to the quartic polynomial fit results.

$$\tau_{zx} = f_{\tau}(\Delta z) = -17.25175 - 0.35747\Delta z + 0.00323\Delta z^2 - 5.97083 \times 10^{-6}\Delta z^3 + 8.02662 \times 10^{-10}\Delta z^4 \tag{15}$$

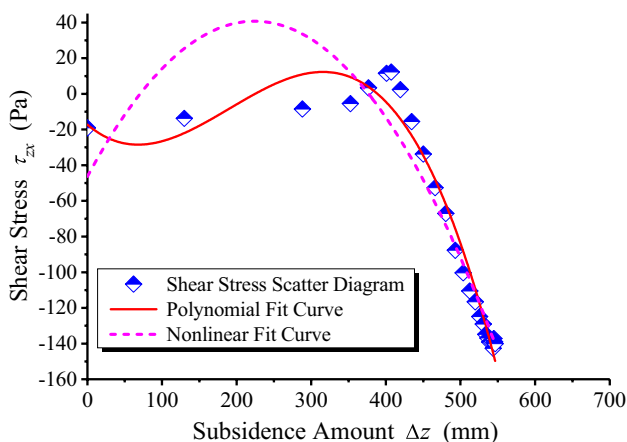


Fig. 16 Fit analysis of subsidence amount and shear stress

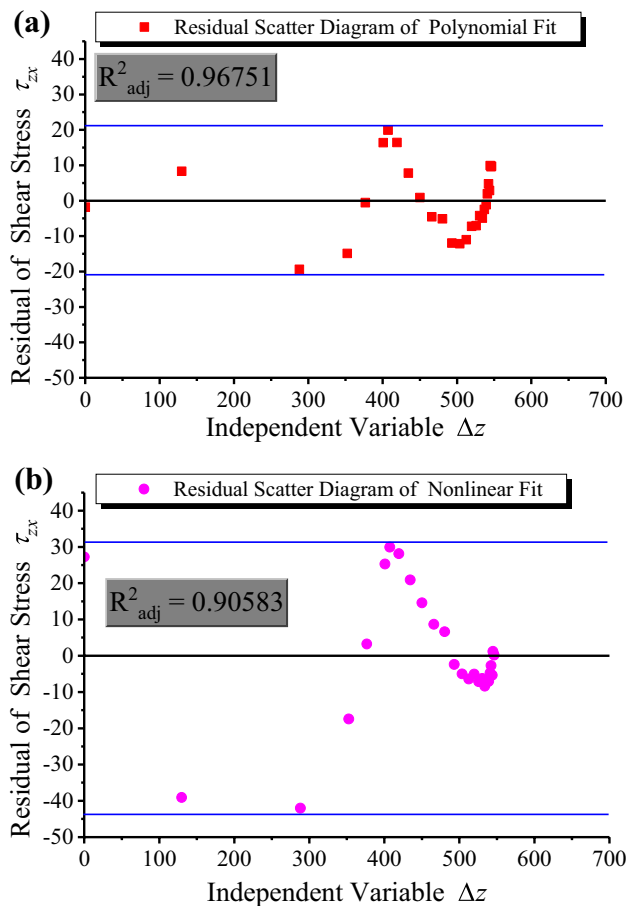


Fig. 17 Residual scatter diagram of shear stress fit analysis: **a** quartic polynomial fit; **b** GaussAmp nonlinear fit

Similarly, the fit function expressions between the subsidence amount Δz and its corresponding shear stress τ_{zx} of other measurement points of clay layer I can be calculated, as shown in Table 3.

2. Relationship between vertical stress σ_z and subsidence amount Δz

The vertical stress σ_z values of each measurement point in clay layer I are shown in Fig. 18 for different advancing distances.

As shown in Fig. 18, the variation trends of the vertical stress distribution curves at different advancing distances are basically the same and the curve distribution is characterized by a high point on both sides of the model and a dip in the middle of the model along the X direction. Meanwhile, the vertical stress increases at each measurement point in clay layer I under the influence of mining, and this increment is 0–10%. Another observation is that with the increase in the advancing distance, the vertical stress increases at both sides along the X direction of the model but decreases at intermediate measurement points.

Taking the advancing distance as the abscissa and the subsidence amount Δz and vertical stress σ_z as the ordinates, there is a corresponding relation between the subsidence amount Δz and vertical stress σ_z , as shown in Fig. 19. This figure shows the corresponding relation between the subsidence and the vertical stress of the $X = 110$ m measurement point in clay layer I.

Hence, a scatter diagram in which the subsidence amount Δz values at the $X = 110$ m measurement point are independent variables and its corresponding vertical stress σ_z values are dependent variables can be plotted. We can then fit and analyse their functional relation and establish their fit function expressions. For instance, Fig. 20 shows the scatter diagram and best-fit curve between the subsidence amount Δz and its corresponding vertical stress σ_z at the $X = 110$ m measurement point. A quartic polynomial [shown in Formula (13)] and GaussAmp nonlinear function [shown in Formula (14)] are used for the fit analysis.

The adjusted determination coefficient R^2_{adj} and residual scatter diagram of the quartic polynomial fit and GaussAmp nonlinear fit analysis are shown in Fig. 21. The results show that the R^2_{adj} and residual values obtained by the quartic polynomial fit and GaussAmp nonlinear fit are similar, illustrating that the fit effects of the quartic polynomial fit and GaussAmp nonlinear fit are similar in the vertical stress fit analysis.

Table 3 Fit Function expressions of subsidence amount and shear stress

Measurement point	Fit function expressions
$X = 50$ m	$\tau_{zx} = f_{\tau}(\Delta z) = -105.60559 - 0.27788\Delta z + 0.00402\Delta z^2 - 1.23526 \times 10^{-5}\Delta z^3 + 7.99761 \times 10^{-9}\Delta z^4$
$X = 110$ m	$\tau_{zx} = f_{\tau}(\Delta z) = -17.25175 - 0.35747\Delta z + 0.00323\Delta z^2 - 5.97083 \times 10^{-6}\Delta z^3 + 8.0266210^{-10}\Delta z^4$
$X = 170$ m	$\tau_{zx} = f_{\tau}(\Delta z) = -126.97266 - 0.05471\Delta z - 0.00253\Delta z^2 + 1.26672 \times 10^{-5}\Delta z^3 - 1.42135 \times 10^{-8}\Delta z^4$
$X = 230$ m	$\tau_{zx} = f_{\tau}(\Delta z) = -144.97653 + 0.50521\Delta z - 0.00746\Delta z^2 + 2.43962 \times 10^{-5}\Delta z^3 - 2.209 \times 10^{-8}\Delta z^4$
$X = 260$ m	$\tau_{zx} = f_{\tau}(\Delta z) = 204.84406 + 0.7639\Delta z - 0.0092\Delta z^2 + 2.88155 \times 10^{-5}\Delta z^3 - 2.55047 \times 10^{-8}\Delta z^4$
$X = 320$ m	$\tau_{zx} = f_{\tau}(\Delta z) = -89.6546 + 1.98509\Delta z - 0.01792\Delta z^2 + 4.98579 \times 10^{-5}\Delta z^3 - 4.18311 \times 10^{-8}\Delta z^4$
$X = 380$ m	$\tau_{zx} = f_{\tau}(\Delta z) = -203.00296 + 0.74186\Delta z - 0.01141\Delta z^2 + 3.55243 \times 10^{-5}\Delta z^3 - 3.05209 \times 10^{-8}\Delta z^4$
$X = 440$ m	$\tau_{zx} = f_{\tau}(\Delta z) = -251.56741 - 1.2285\Delta z + 0.01179\Delta z^2 - 4.02181 \times 10^{-5}\Delta z^3 + 4.49153 \times 10^{-8}\Delta z^4$

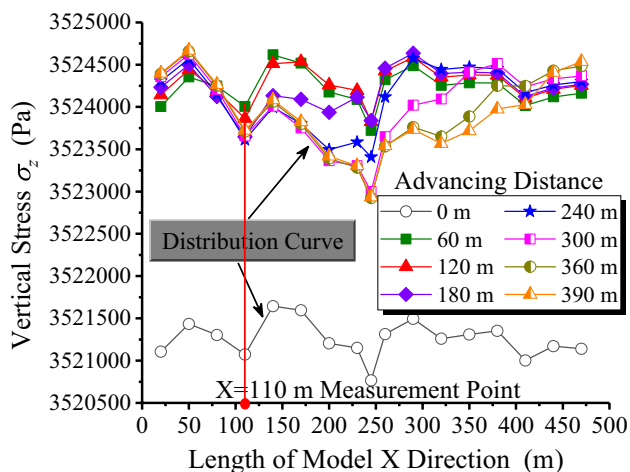


Fig. 18 Vertical stress values of each measurement point in clay layer I

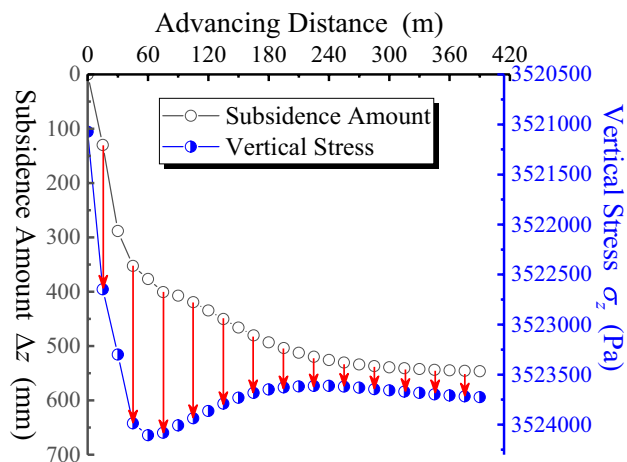


Fig. 19 The relationship between subsidence amount and vertical stress

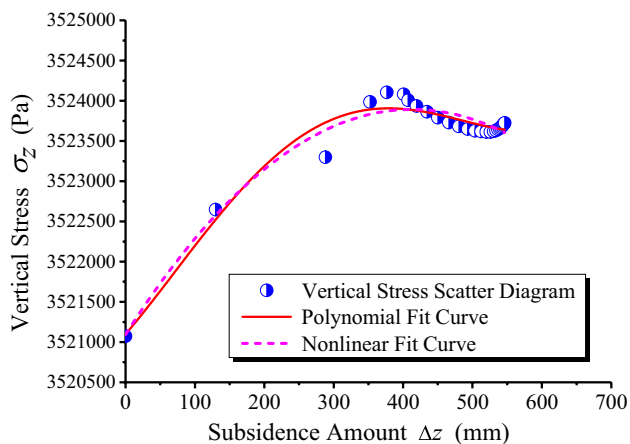


Fig. 20 Fit analysis of subsidence amount and vertical stress

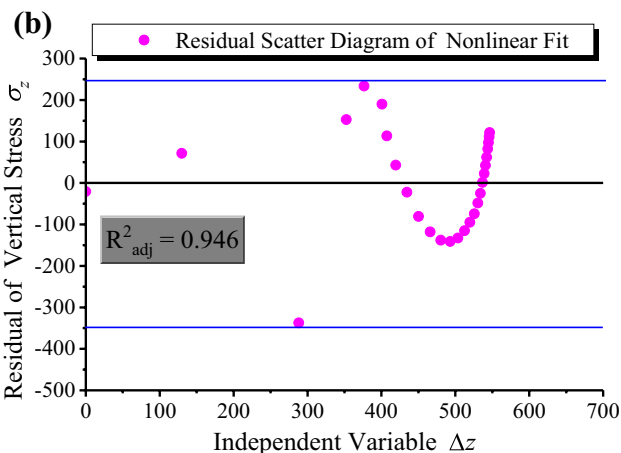
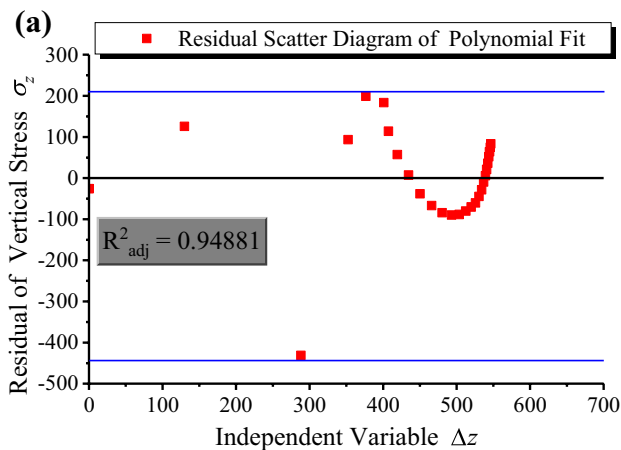


Fig. 21 Residual scatter diagram of the vertical stress fit analysis: a quartic polynomial fit; b GaussAmp nonlinear fit

The fit function expressions between subsidence amount Δz and vertical stress σ_z at $X = 110$ m measurement point is shown in Formula (16) according to the quartic polynomial fit results.

$$\sigma_z = f_z(\Delta z) = 3.5211 \times 10^6 + 10.00473\Delta z + 0.01948\Delta z^2 - 1.05448 \times 10^{-4}\Delta z^3 + 9.49403 \times 10^{-8}\Delta z^4. \quad (16)$$

In the same way, we can calculate the fit function expressions between the subsidence amount Δz and its corresponding vertical stress σ_z at other measurement points of clay layer I, as shown in Table 4.

(3) Relationship between horizontal stress σ_x and subsidence amount Δz

The horizontal stress σ_x values of each measure point in clay layer I at different advancing distances are shown in Fig. 22.

As shown in Fig. 22, the horizontal stress at each measurement point is basically constant when the advancing distance is less than 60 m, while it clearly varies when the advancing distance is greater than 120 m. Meanwhile, the

Table 4 Fit Function expressions of subsidence amount and vertical stress

Measurement point	Fit function expressions
X=50 m	$\sigma_z = f_z(\Delta z) = 3.52143 \times 10^6 + 12.36031\Delta z + 0.02084\Delta z^2 - 1.68502 \times 10^{-4}\Delta z^3 + 2.15482 \times 10^{-7}\Delta z^4$
X=110 m	$\sigma_z = f_z(\Delta z) = 3.5211 \times 10^6 + 10.00473\Delta z + 0.01948\Delta z^2 - 1.05448 \times 10^{-4}\Delta z^3 + 9.49403 \times 10^{-8}\Delta z^4$
X=170 m	$\sigma_z = f_z(\Delta z) = 3.52161 \times 10^6 + 6.07338\Delta z + 0.05219\Delta z^2 - 1.81654 \times 10^{-4}\Delta z^3 + 1.46354 \times 10^{-7}\Delta z^4$
X=230 m	$\sigma_z = f_z(\Delta z) = 3.52116 \times 10^6 + 6.12089\Delta z + 0.04968\Delta z^2 - 1.6765 \times 10^{-4}\Delta z^3 + 1.29934 \times 10^{-7}\Delta z^4$
X=260 m	$\sigma_z = f_z(\Delta z) = 3.52134 \times 10^6 + 6.33927\Delta z + 0.04376\Delta z^2 - 1.45122 \times 10^{-4}\Delta z^3 + 1.08756 \times 10^{-7}\Delta z^4$
X=320 m	$\sigma_z = f_z(\Delta z) = 3.5213 \times 10^6 + 7.46526\Delta z + 0.02831\Delta z^2 - 9.62481 \times 10^{-5}\Delta z^3 + 6.54297 \times 10^{-8}\Delta z^4$
X=380 m	$\sigma_z = f_z(\Delta z) = 3.52136 \times 10^6 + 8.77866\Delta z + 0.00503\Delta z^2 - 1.0412 \times 10^{-5}\Delta z^3 - 2.22977 \times 10^{-8}\Delta z^4$
X=440 m	$\sigma_z = f_z(\Delta z) = 3.52117 \times 10^6 + 26.55482\Delta z - 0.17188\Delta z^2 + 5.30583 \times 10^{-4}\Delta z^3 - 5.42645 \times 10^{-7}\Delta z^4$

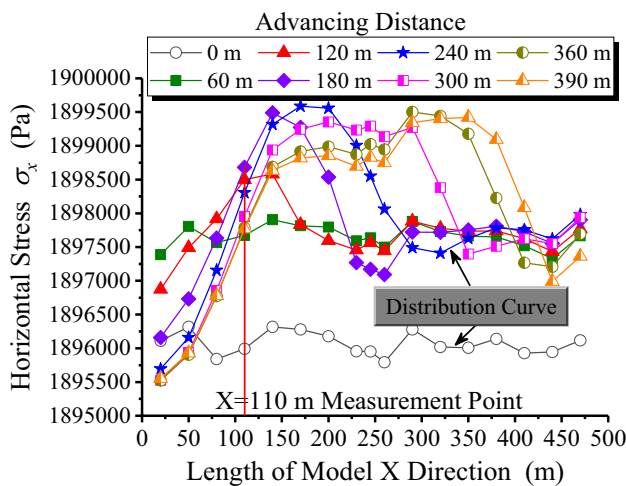


Fig. 22 Horizontal stress values of each measurement point in clay layer I

horizontal stress distribution is characterized by the lows on both sides of the model and a high in the middle along the X direction of the model. Another observation is that the horizontal stress increases at most of the measurement points in clay layer I under the influence of mining, and the variation is $-0.03\text{--}0.18\%$. In contrast, the variation in the vertical stress affected by mining is $0\text{--}0.10\%$, and the corresponding variation in the shear stress is $-82.16\text{--}634.16\%$, which illustrates that coal mining has the greatest influence on shear stress, followed by horizontal stress, with the smallest effect on vertical stress.

Taking the advancing distance as the abscissa and the subsidence amount Δz and horizontal stress σ_x as the ordinates, and there is a corresponding relation between subsidence amount Δz and horizontal stress σ_x , as shown in Fig. 23. This figure shows the corresponding relationship between the subsidence amount and the horizontal stress at the X=110 m measurement point in clay layer I.

Hence, a scatter diagram can be plotted in which the subsidence amount Δz values at the X=110 m measurement point are independent variables and its corresponding

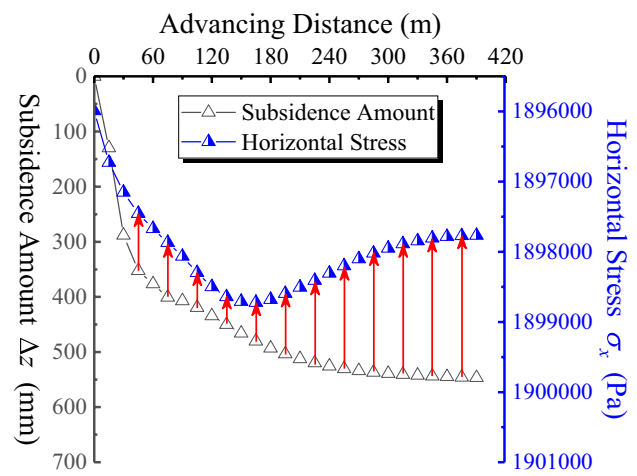


Fig. 23 The relationship between subsidence amount and horizontal stress

horizontal stress σ_x values are dependent variables. We can then fit and analyse their functional relation and establish their fit function expressions. For instance, the scatter diagram and best-fit curve between subsidence amount Δz and its corresponding horizontal stress σ_x at the X=110 m measurement point are shown in Fig. 24. A quartic polynomial [as shown in Formula (13)] and GaussAmp nonlinear function [as shown in Formula (14)] are used for the fit analysis.

The adjusted determination coefficient R_{adj}^2 and residual scatter diagram of the quartic polynomial fit and GaussAmp nonlinear fit analysis are shown in Fig. 25. The R_{adj}^2 determined by the quartic polynomial fit is greater than that of the GaussAmp nonlinear fit, while the residual values of the quartic polynomial fit are lesser than those of the GaussAmp nonlinear fit, illustrating that the quartic polynomial fit has a better fit effect than the GaussAmp nonlinear fit in the horizontal stress fit analysis.

The fit function expressions between subsidence amount Δz and horizontal stress σ_x at the X=110 m measurement

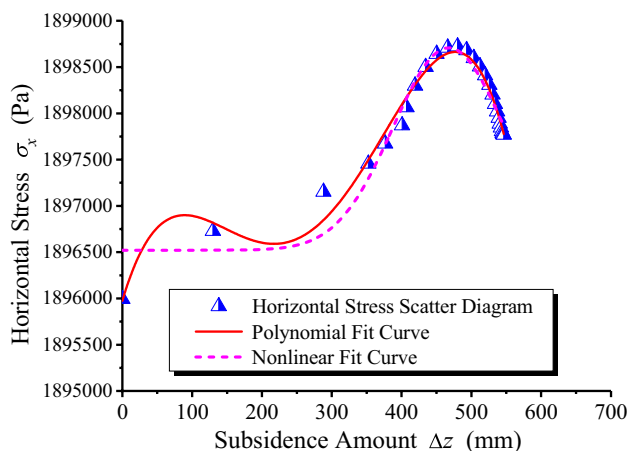


Fig. 24 Fit analysis of subsidence amount and horizontal stress

point is shown in Formula (17) according to the quartic polynomial fit results.

$$\sigma_x = f_x(\Delta z) = 1.89597 \times 10^6 + 25.47879\Delta z - 0.228\Delta z^2 + 7.19305 \times 10^{-4}\Delta z^3 - 6.88724 \times 10^{-7}\Delta z^4. \quad (17)$$

Similarly, we can calculate the fit function expressions between the subsidence amount Δz and its corresponding vertical stress σ_x at other measurement points in clay layer I, as shown in Table 5.

(4) Soil failure criterion expressed by subsidence amount Δz

The soil failure criterion expressed by subsidence amount Δz can be obtained if the τ_{zx} (shown in Table 3), σ_z (shown in Table 4) and σ_x (shown in Table 5) are substituted into Formula (12). For example, σ_z , σ_x and τ_{zx} at the $X = 110$ m measurement point are substituted into Formula (12). Then, the failure criterion expressed by Δz is obtained, as shown in Formula (18).

$$\begin{aligned} & (1-\zeta^2)(2.708535 \times 10^6 + 17.74176\Delta z - 0.10426\Delta z^2 + 3.069285 \times 10^{-4}\Delta z^3 - 2.9689185 \times 10^{-7}\Delta z^4) \\ & + (1+\zeta^2) \sqrt{(8.12565 \times 10^5 - 7.73703\Delta z + 0.12374\Delta z^2 - 4.123765 \times 10^{-4}\Delta z^3 + 3.9183215 \times 10^{-7}\Delta z^4)^2} \\ & - 2c\zeta < 0 \end{aligned} \quad (18)$$

Formula (18) is a discriminant formula for the conditions that subsidence amount Δz should satisfy when the clay is not in a state of failure.

Procedure of the soil failure discriminant method

On the basis of the measured cohesion c and internal friction angle φ of clay, the failure subsidence amount satisfies Formula (18) can be obtained, and the failure subsidence

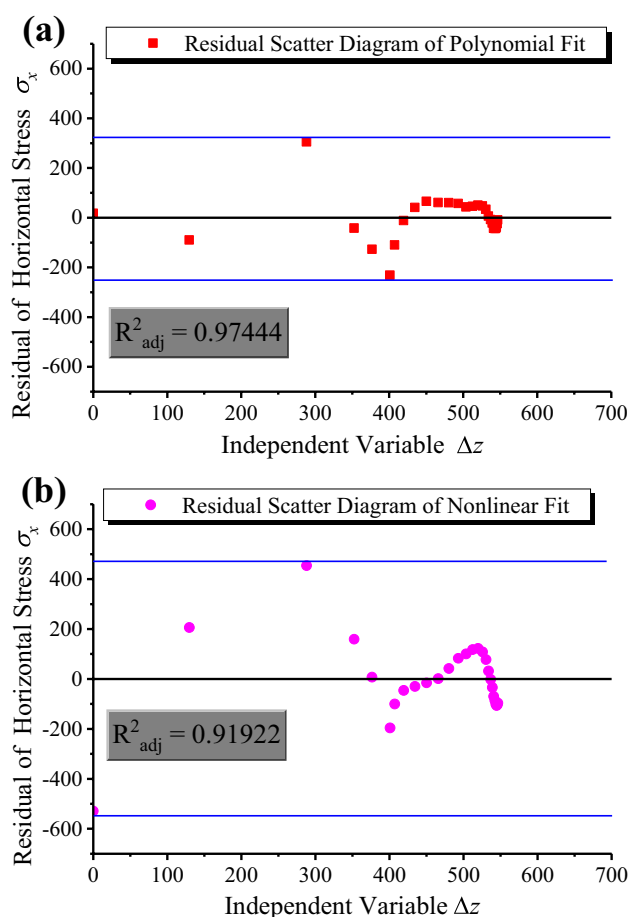


Fig. 25 Residual scatter diagram of the horizontal stress fit analysis: a quartic polynomial fit; b GaussAmp nonlinear fit

amount curve can be drawn. Then, the failure subsidence amount curve can be compared with the actual subsidence amount curve of the soil to judge whether the soil is in a state of failure.

Here, we summarize the above-mentioned methods and main steps. The procedure of the soil failure discriminant method is shown in Fig. 26.

The ultimate goal of this method is to establish the expressions of the soil failure criterion expressed by the subsidence amount; therefore, it is only necessary to determine the subsidence amount to judge the failure state of the overlying clay layer, and determining whether the overlying clay layer fails or does not have a great influence on

Table 5 Fit Function expressions of subsidence amount and horizontal stress

Measurement point	Fit function expressions
X=50 m	$\sigma_x = f_x(\Delta z) = 1.89632 \times 10^6 + 27.66691\Delta z - 0.30947\Delta z^2 + 0.00123\Delta z^3 - 1.54434 \times 10^{-6}\Delta z^4$
X=110 m	$\sigma_x = f_x(\Delta z) = 1.89597 \times 10^6 + 25.47879\Delta z - 0.228\Delta z^2 + 7.19305 \times 10^{-4}\Delta z^3 - 6.88724 \times 10^{-7}\Delta z^4$
X=170 m	$\sigma_x = f_x(\Delta z) = 1.89623 \times 10^6 + 27.28579\Delta z - 0.19953\Delta z^2 + 5.23625 \times 10^{-4}\Delta z^3 - 4.2069 \times 10^{-7}\Delta z^4$
X=230 m	$\sigma_x = f_x(\Delta z) = 1.89588 \times 10^6 + 27.33263\Delta z - 0.1743\Delta z^2 + 4.10634 \times 10^{-4}\Delta z^3 - 3.01609 \times 10^{-7}\Delta z^4$
X=260 m	$\sigma_x = f_x(\Delta z) = 1.89573 \times 10^6 + 23.98683\Delta z - 0.14627\Delta z^2 + 3.38771 \times 10^{-4}\Delta z^3 - 2.44225 \times 10^{-7}\Delta z^4$
X=320 m	$\sigma_x = f_x(\Delta z) = 1.89598 \times 10^6 + 16.87587\Delta z - 0.08424\Delta z^2 + 1.76222 \times 10^{-4}\Delta z^3 - 1.11778 \times 10^{-7}\Delta z^4$
X=380 m	$\sigma_x = f_x(\Delta z) = 1.89616 \times 10^6 - 3.74586\Delta z + 0.10828\Delta z^2 - 3.75082 \times 10^{-4}\Delta z^3 + 3.78956 \times 10^{-7}\Delta z^4$
X=440 m	$\sigma_x = f_x(\Delta z) = 1.89595 \times 10^6 + 19.64234\Delta z - 0.19309\Delta z^2 + 7.17097 \times 10^{-4}\Delta z^3 - 8.33489 \times 10^{-7}\Delta z^4$

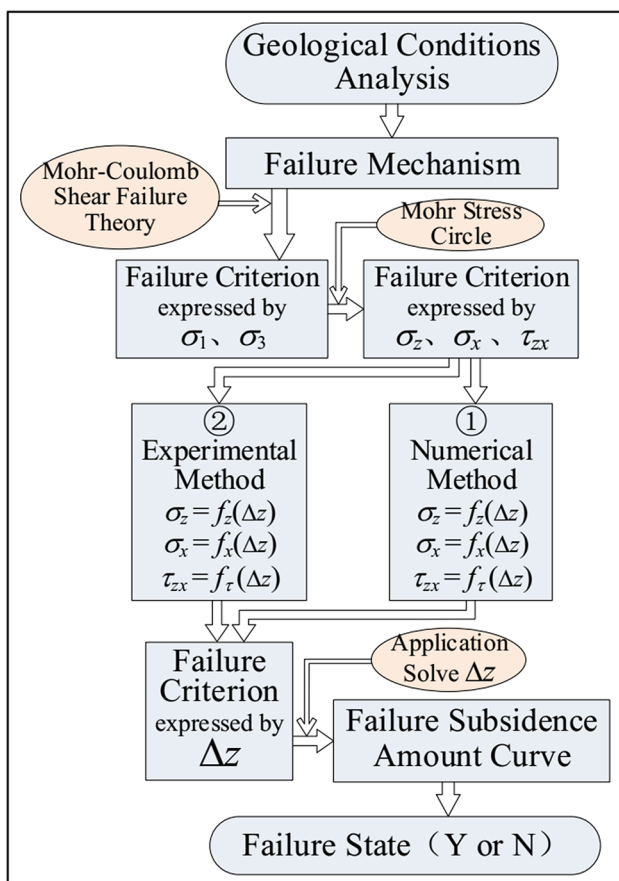


Fig. 26 Procedure of the soil failure discriminant method

Table 6 Failure subsidence amount of clay layer I

Measurement point	Failure subsidence amount
X=50 m	1050.33 mm ≤ Δz
X=110 m	1310.64 mm ≤ Δz
X=170 m	1480.74 mm ≤ Δz
X=230 m	1664.74 mm ≤ Δz
X=260 m	1671.35 mm ≤ Δz
X=320 m	1966.71 mm ≤ Δz
X=380 m	2223.62 mm ≤ Δz
X=440 m	1475.92 mm ≤ Δz

the safe mining and protection of underground latent water resources. This study provides a new method to distinguish whether the overlying clay layer is fails, to better protect underground latent water resources.

Engineering application

Calculation of the failure subsidence amount of the clay

The 3301 working face was the first mining face and is located in eastern mining area No. 3, which is an area with the thinnest bedrock. In most areas of the 3301 working face, the bedrock thickness is less than 50 m, while the thickness of the Quaternary overburden is greater than 200 m. The cohesion *c* and internal friction angle *φ* of the clay in mining area No. 3 have been obtained and are shown in Table 1. For instance, *c* = 104500 Pa and *φ* = 29.1° are substituted into Formula (18) to obtain Formula (19).

$$\begin{aligned}
 & -1.89359111 \left(2.708535 \times 10^6 + 17.74176\Delta z - 0.10426\Delta z^2 + 3.069285 \times 10^{-4}\Delta z^3 - 2.9689185 \times 10^{-7}\Delta z^4 \right) \\
 & + 3.89359111 \sqrt{ \left(8.12565 \times 10^5 - 7.73703\Delta z + 0.12374\Delta z^2 - 4.123765 \times 10^{-4}\Delta z^3 + 3.9183215 \times 10^{-7}\Delta z^4 \right)^2 } \\
 & + \left(-17.25175 - 0.35747\Delta z + 0.00323\Delta z^2 - 5.97083 \times 10^{-6}\Delta z^3 + 8.02662 \times 10^{-10}\Delta z^4 \right)^2 } \\
 & - 355520.679 < 0
 \end{aligned} \tag{19}$$

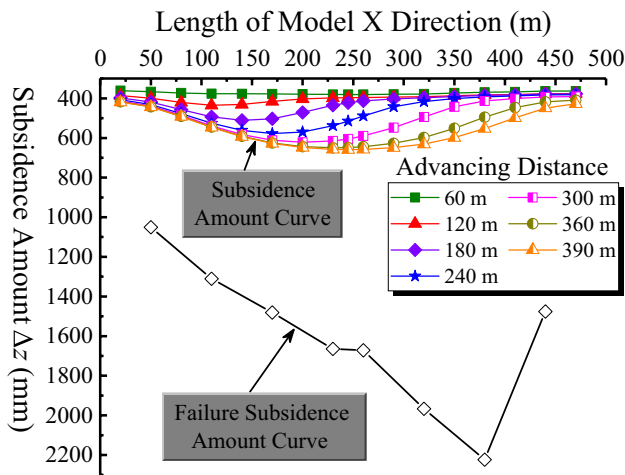


Fig. 27 Discrimination diagram of clay failure

Solving Formula (19) obtains $-785.14 \text{ mm} < \Delta z < 1310.64 \text{ mm}$, which means that clay layer I will not fail at $X = 110 \text{ m}$ if the subsidence amount Δz satisfies the condition $\Delta z < 1310.64 \text{ mm}$. That is, clay layer I will fail at $X = 110 \text{ m}$ when the subsidence amount is greater than or

equal to 1310.64 mm . Similarly, the calculated failure subsidence amount at the other measurement points of clay layer I are shown in Table 6.

The failure subsidence amount in Table 6 are plotted in Fig. 27 to obtain the failure subsidence amount curve of clay layer I. Then, the failure state of clay layer I can be judged according to the relative relation between the failure subsidence amount curve and the subsidence amount curve. If the failure subsidence amount curve plots below the subsidence amount curves at any advancing distance, that is, the mining subsidence amount of the clay layer is less than its failure subsidence amount, the clay layer will not fail. When the failure subsidence amount curve plots above the subsidence amount curves at any advancing distance, the mining subsidence amount of the clay layer is greater than its failure subsidence amount, and the clay layer will fail.

According to Fig. 27, the subsidence amount at each measurement point of clay layer I is less than the failure subsidence amount. This result indicates that clay layer I at the bottom of the Quaternary system in mining area No. 3 is within the safe subsidence amount range and that clay layer I does not fail during coal seam mining.

Table 7 Water quality test results of the Quaternary cover layer water sample

Cation	Content (mmol/L)	Proportion (%)	Anion	Content (mmol/L)	Proportion (%)
K ⁺	0.021	0.119	Cl ⁻	7.990	45.154
Na ⁺	4.249	24.012	SO ₄ ²⁻	4.103	23.187
Ca ²⁺	8.031	45.386	HCO ₃ ⁻	5.187	29.313
Mg ²⁺	5.394	30.483	CO ₃ ²⁻	0.202	1.142
Fe ³⁺	0.000	0.00	NO ₃ ⁻	0.210	1.187
Fe ²⁺	0.000	0.00	NO ₂ ⁻	0.003	0.017
NH ₄ ⁺	0.000	0.00	PO ₄ ³⁻	0.000	0.00
Total	17.695	100	Total	17.695	100
Total hardness 671.81 mg/L			Total dissolved solid 982.00 mg/L		
Total alkalinity 2.538			pH value 8.15		

Table 8 Water quality test results of the bedrock section water sample

Cation	Content (mmol/L)	Proportion (%)	Anion	Content (mmol/L)	Proportion (%)
K ⁺	0.046	0.360	Cl ⁻	3.601	28.192
Na ⁺	1.467	11.485	SO ₄ ²⁻	3.882	30.392
Ca ²⁺	7.679	60.119	HCO ₃ ⁻	5.284	41.369
Mg ²⁺	3.581	28.036	CO ₃ ²⁻	0.000	0.00
Fe ³⁺	0.000	0.00	NO ₃ ⁻	0.000	0.00
Fe ²⁺	0.000	0.00	NO ₂ ⁻	0.006	0.047
NH ₄ ⁺	0.000	0.00	PO ₄ ³⁻	0.000	0.00
Total	12.773	100	Total	12.773	100
Total hardness 563.43 mg/L			Total dissolved solid 705.00 mg/L		
Total alkalinity 2.644			pH value 7.89		

Source and amount of water inflow in the working face

1. Source of water inflow in the working face

It is more accurate and appropriate to verify the above-mentioned soil failure discriminant method with field measurement data of stress and deformations. Because of the large amount of work and the long time required for field testing of the internal subsidence and stress of the soil, at present, only the water quality test and water inflow amount results from the 3301 working face were used to identify the source of water gushing into the working face, thus indirectly verifying whether the soil is in a state of failure.

The water samples from the porous aquifers (6.05–188.78 m) in the Quaternary cover layer and the fractured aquifers (188.78–245.00 m) in the bedrock section were collected before mining of the 3301 working face. Then, the samples were sent to the 212 Geological Laboratory of the Geological and Mineral Resources Bureau of Shanxi Province to carry out the water quality laboratory tests, and the results are shown in Tables 7 and 8.

The water samples from the water gushing point in the 3301 working face were collected when the 3301 working face was being mined (as shown in Fig. 28), and the water quality test results are shown in Table 9.

Tables 7, 8 and 9 list the results of the indicators, such as the pH value, total hardness, and ion content, at different specimen sites. According to the test results, the water quality types of the porous aquifers in the Quaternary cover layer, fractured aquifers in the bedrock section and gushing point in the 3301 working face are $\text{Cl} \cdot \text{HCO}_3 - \text{Ca} \cdot \text{Mg}$, $\text{HCO}_3 \cdot \text{SO}_4 \cdot \text{Cl} - \text{Ca} \cdot \text{Mg}$, and $\text{HCO}_3 \cdot \text{SO}_4 \cdot \text{Cl} - \text{Ca}$, respectively. The water quality of the water from the gushing point in the 3301 working face is similar to that from the fractured aquifers in the bedrock section but is different from the porous aquifers in the Quaternary cover layer according to the indicator values of the water quality and water quality type.

These results show that the main source of water gushing in the 3301 working face is the fractured aquifers in the bedrock section and that the clay layer at the bottom of the Quaternary overburden blocks the hydraulic connection between the Quaternary cover layer porous aquifers and the working face. Moreover, this indirectly indicates that the clay layer of the Quaternary cover layer did not fail under the condition of thin bedrock (the coal seam thickness is 7.0 m, and the bedrock thickness ranges from 48.84 to 52.73 m).

2. Amount of water inflow in the working face

During the 3301 working face mining process, the amount of water inflow from the working face is observed, and the results are shown in Fig. 29.

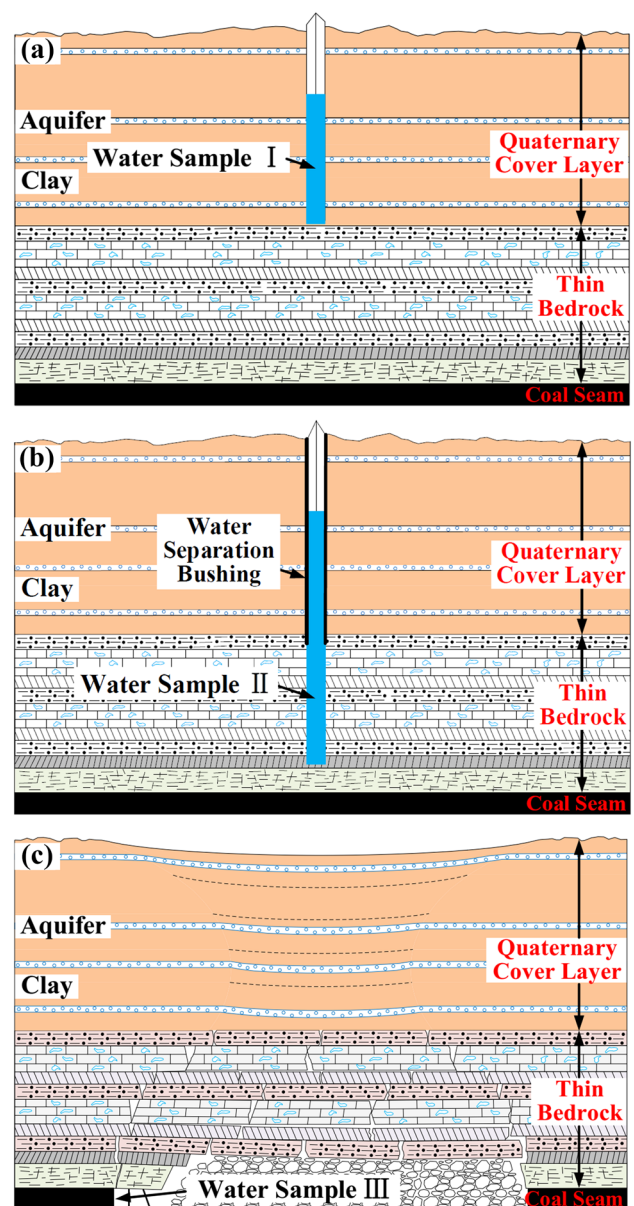


Fig. 28 Source of water specimens: **a** water sample taken from the Quaternary cover layer; **b** water sample taken from the bedrock section; **c** water sample taken from the working face

Figure 29 shows that the amounts of water inflow at the 3301 working face are relatively small in each month, and there is no obvious change with the increase in the working face advancing distance. Therefore, there is only one source of water (water in fractured aquifers in the bedrock section) gushing into the 3301 working face, illustrating that the water from the Quaternary cover layer porous aquifers and from the surface ponds are not greatly gushing into the working face. This indirectly indicates that the clay layer in the Quaternary cover layer did not fail under the condition of thin bedrock (the coal seam thickness is 7.0 m, and the bedrock thickness ranges from 48.84 to 52.73 m).

Table 9 Water quality test results of the water sample taken from 3301 working face

Cation	Content (mmol/L)	Proportion (%)	Anion	Content (mmol/L)	Proportion (%)
K ⁺	0.053	0.414	Cl ⁻	3.296	25.718
Na ⁺	1.074	8.380	SO ₄ ²⁻	3.928	30.649
Ca ²⁺	8.531	66.565	HCO ₃ ⁻	5.585	43.578
Mg ²⁺	3.158	24.641	CO ₃ ²⁻	0.000	0.00
Fe ³⁺	0.000	0.00	NO ₃ ⁻	0.000	0.00
Fe ²⁺	0.000	0.00	NO ₂ ⁻	0.007	0.055
NH ₄ ⁺	0.000	0.00	PO ₄ ³⁻	0.000	0.00
Total	12.816	100	Total	12.816	100

Total hardness: 583.27 mg/L
 Total alkalinity: 2.574
 Total dissolved solid: 813.00 mg/L
 pH value: 7.93

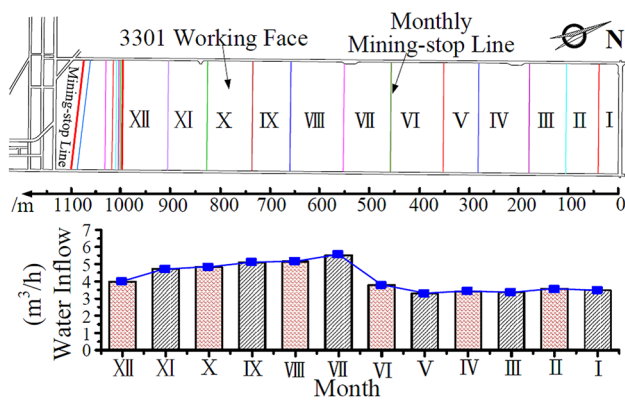


Fig. 29 Mining progress and water inflow of the 3301 working face

Conclusion

1. The soil failure criterion expressed by vertical stress, horizontal stress and shear stress is derived based on the Mohr–Coulomb shear failure theory. Under the condition of thin bedrock, the mining of coal seam results in the reduction in the supporting space in the lower part of the overlying soil layers, which will subside due to the self-weight load. Consequently, the vertical stress, horizontal stress and shear stress of the soil changed before the overlying soil layers were re-compacted on the collapsed or cracked thin bedrock, and the change of vertical stress, horizontal stress and shear stress determined whether the soil was failing.
2. The fit function relation between the soil subsidence amount and vertical stress, horizontal stress, and shear stress is established through numerical analysis. Then, the expressions of the soil failure criterion expressed by the soil subsidence amount are derived. Based on this work, a procedure of the soil failure discriminant method is proposed, in which only the soil subsidence amount is necessary to judge the failure state of soil,

providing a new method to distinguish whether the soil is in a state of failure.

3. Soil failure subsidence amount is calculated according to the actual geological conditions of the SanYuan Coal Mine, and the failure subsidence amount curve is drawn. The results show that the failure subsidence amount curve plots below the subsidence amount curves at any advancing distance; that is, the mining subsidence amount of the clay layer is less than its failure subsidence amount, and the clay layer is not failing. Combined with information on the source and amount of water inflow at the 3301 working face, it is also verified that the clay layer did not fail, and the soil failure discriminant method used to judge the failure state of the soil is appropriate.

References

Arkoc O, Ucar S, Ozcan C (2016) Assessment of impact of coal mining on ground and surface waters in Tozaklı coal field, Kırklareli, northeast of Thrace, Turkey. *Environ Earth Sci* 75:514

Bai HB, Ma D, Chen ZQ (2013) Mechanical behavior of groundwater seepage in karst collapse pillars. *Eng Geol* 164:101–106

Chen XZ (1997) *Foundation of soil mechanics*. Tsinghua University Press, Beijing

Dhakate R, Singh VS, Hodlur GK (2008) Impact assessment of chromite mining on groundwater through simulation modeling study in Sukinda chromite mining area, Orissa, India. *J Hazard Mater* 160:535–547

Dong QH, Cai R (2006) Deformation Simulation and Affection Analysis of Clay Layer Under Unconsolidated Water-bearing Strata during Mining. *Energy Technol Manag* 6:53–60

Du F, Bai HB, Huang HF, Jiang GH (2013) Mechanical analysis of periodic weighting of main roof in longwall top coal caving face with thin bedrock roof. *J China Univ Min Technol* 42(3):362–369

Fan LM (2005) Discussing on coal mining under water-containing condition. *Coal Geol Explor* 33(5):50–53

Fan LM (2011) Development of coal mining method with water protection in fragile ecological region. *J Liaoning Tech Univ (Nat Sci)* 30(5):667–671

- Fan LM, Wang SM, Ma XD (2009) Typical example of new idea for water conservation and coal mining. *Min Sa Environ Prot* 36(1):61–65
- Fang XQ, Huang HF, Jin T, Bai JB (2008) Movement rules of overlying strata around longwall mining in thin bedrock with thick surface soil. *Chin J Rock Mech Eng* 27(supplement 1):2700–2706
- Jiao Y, Bai HB, Zhang BY, Wei XQ, Rong HR (2012) Research on the effect of coal mining on the aquifer of quaternary loose soils. *J Ming Saf Eng* 29(2):239–244
- Li WP, Wang QQ, Li XQ (2017) Reconstruction of aquifuge: the engineering geological study of N2 laterite located in key aquifuge concerning coal mining with water protection in Northwest China. *J China Coal Soc* 42(1):88–96
- Liu SQ (2016) The law of the overburden failure in thick coal seam mining and instability criterion of the clay aquiclude under the influence of mining. China University of Mining & Technology, Beijing
- Ma D, Miao X, Bai H, Pu H, Chen Z, Liu J, Huang Y, Zhang G, Zhang Q (2016a) Impact of particle transfer on flow properties of crushed mudstones. *Environ Earth Sci* 75:593
- Ma D, Miao X, Bai H, Huang J, Pu H, Wu Y, Zhang G, Li J (2016b) Effect of mining on shear sidewall groundwater inrush hazard caused by seepage instability of the penetrated karst collapse pillar. *Nat Hazards* 82(1):73–93
- Ma D, Rezanian M, Yu H-S, Bai H-B (2017) Variations of hydraulic properties of granular sandstones during water inrush: effect of small particle migration. *Eng Geol* 217:61–70
- Ma D, Cai X, Li Q, Duan H (2018) In-situ and numerical investigation of groundwater inrush hazard from grouted karst collapse pillar in longwall mining. *Water* 10(9):1187
- Ma D, Duan H, Liu J, Li X, Zhou Z (2019) The role of gangue on the mitigation of mining-induced hazards and environmental pollution: an experimental investigation. *Sci Total Environ* 664:436–448
- Meng ZP, Gao YF, Lu AH, Wang R, Qiao X, Huang CY (2013) Water inrush risk evaluation of coal mining under quaternary alluvial water and reasonable design method of waterproof coal pillar. *J Min Saf Eng* 30(1):23–29
- Palchik V (2003) Formation of fractured zones in overburden due to longwall mining. *Environ Geol* 44:28–38
- Qian MG (2010) On sustainable coal mining in China. *J China Coal Soc* 35(4):529–534
- Qian MG, Xu JL, Miao XX (2003) Green technique in coal mining. *J China Univ Min Technol* 32(4):343–347
- Qian MG, Miao XX, Xu JL (2006) Resources and environment harmonics (Green) mining and its technological system. *J Min Saf Eng* 23(1):1–5
- Qiao W, Li WP, Li T, Chang JY, Wang QQ (2017) Effects of coal mining on shallow water resources in semiarid regions: a case study in the Shennan Mining Area, Shaanxi, China. *Mine Water Environ* 36:104–113
- Su D (2015) Soil mechanics. Tsinghua University Press, Beijing
- Sun XK, Ma GJ, Xu XQ (2004) Analysis of influence of quaternary bottom boundary clay lithology on improving mining upper limit. *Saf Coal Mines* 35(6):31–33
- Tiwary RK (2001) Environmental impact of coal mining on water regime and its management. *Water Air Soil Pollut* 132:185–199
- Xu YC (2004a) Engineering characteristics of deep clay and its application in coal mining under building structure, railway and water body. *Coal Sci Technol* 32(11):21–23
- Xu YC (2004b) Mechanics characteristics of deep saturated clay. *J China Coal Soc* 29(1):26–30
- Xu YC, Luo YQ, Li JH, Li KQ, Cao XC (2018) Water and sand inrush during mining under thick unconsolidated layers and thin bedrock in the Zhaogu No. 1 Coal Mine, China. *Mine Water Environ* 37:336–345
- Xuan YQ (2008) Research on movement and evolution law of breaking of overlying strata in shallow coal seam with a thin bedrock. *Rock Soil Mech* 29(2):512–516
- Yang WF, Xia XH (2013) Prediction of mining subsidence under thin bedrocks and thick unconsolidated layers based on field measurement and artificial neural networks. *Comput Geosci* 52:199–203
- Yang WF, Xia XH (2018) Study on mining failure law of the weak and weathered composite roof in a thin bedrock working face. *J Geophys Eng* 15:2370–2377
- Zhang MS, Dong Y, Du RJ, Xiao XF (2010a) The strategy and influence of coal mining on the groundwater resources at the energy and chemical base in the North of Shanxi. *Earth Sci Front* 17(6):235–246
- Zhang LZ, Dong QH, Zhang XC, Gao XT, Zhan KY (2010b) Study on self healing ability of mining fissure of loose layer remolded clay. *Energy Technol Manag* 1:57–60
- Zhang DS, Fan GW, Ma LQ, Wang XF (2011) Aquifer protection during longwall mining of shallow coal seams: a case study in the Shendong Coalfield of China. *Int J Coal Geol* 86:190–196
- Zhang JM, Li QS, Nan QA, Cao ZG, Zhang K (2017) Study on the bionic coal & water co-mining and its technological system in the ecological fragile region of West China. *J China Coal Soc* 42(1):66–72
- Zhang SZ, Fan GW, Zhang DS, Li QZ (2018) Physical simulation research on evolution laws of clay aquifuge stability during slice mining. *Environ Earth Sci* 77:278
- Zhou DW, Wu K, Li L, Diao XP, Kong XS (2016) A new methodology for studying the spreading process of mining subsidence in rock mass and alluvial soil: an example from the Huainan coal mine, China. *Bull Eng Geol Env* 75:1067–1087
- Zhou Z, Cai X, Ma D, Chen L, Wang S, Tan L (2018a) Dynamic tensile properties of sandstone subjected to wetting and drying cycles. *Constr Build Mater* 182:215–232
- Zhou Z, Cai X, Ma D, Cao W, Chen L, Zhou J (2018b) Effects of water content on fracture and mechanical behavior of sandstone with a low clay mineral content. *Eng Fract Mech* 193:47–65
- Zhou Z, Cai X, Ma D, Du X, Chen L, Wang H, Zang H (2019) Water saturation effects on dynamic fracture behavior of sandstone. *Int J Rock Mech Min Sci* 114:46–61

Publisher's Note Springer Nature remains neutral with regard to jurisdictional claims in published maps and institutional affiliations.